Comparison of global Joule heating estimates in GITM, TIE-GCM and empirical formulations during St. Patrick's Day 2015 geomagnetic storm

Panagiotis Pirnaris[1], Theodoros Sarris[1], Stelios Tourgaidis[1]and Aaron Ridley[2]

[1]Department of Electrical and Computer Engineering, Democritus University of Thrace
[2]Department of Atmosphere, Oceanic and Space Sciences, University of Michigan

Key Points:

- Joule heating in the Earth's Lower Thermosphere-Ionosphere is estimated and compared in GITM, TIE-GCM and empirical models.
- Joule heating estimates in GITM and TIE-GCM exceed the corresponding estimates via empirical models.
- The correlation of Joule heating to various solar and geomagnetic indices is largely different between GITM, TIE-GCM.
- Significant differences are found in the evolution, dependence, localization and hemispherically-integrated Joule heating between GITM and TIE-GCM.

Corresponding author: Theodoros Sarris, tsarris@ee.duth.gr

Corresponding author: Panagiotis Pirnaris, ppyrnar@ee.duth.gr, ppyrnar@ee.duth.gr

Abstract

It is well known that the primary solar wind energy dissipation mechanism in the Earth's upper atmosphere is Joule heating. Two of the most commonly used physics-based Global Circulation Models (GCM) of the Earth's upper atmosphere are the Global Ionosphere/ Thermosphere Model (GITM) and the Thermosphere-Ionosphere-Electrodynamics General Circulation Model (TIE-GCM). At the same time, a number of empirical formulations have been derived to provide estimates of Joule heating rates based on indices of solar and geomagnetic activity. In this paper, a comparison of the evolution of the globally-integrated Joule heating rates between the two GCMs and various empirical formulations is performed during the solar storm of 17 March 2015. It is found that all empirical formulations on average underestimate Joule heating rates compared to both GITM and TIE-GCM, whereas TIE-GCM calculates lower heating rates compared to GITM. It is also found that Joule heating is primarily correlated with the auroral electrojet in GITM, whereas Joule heating in TIE-GCM is correlated better with the *Dst* index and with prolonged southward turnings of the Interplanetary Magnetic Field component, B_z. By calculating the heating rates separately in the northern and southern hemispheres it is found that in GITM higher Joule heating rates are observed in the northern hemisphere, whereas in TIE-GCM higher Joule heating rates are observed in the southern hemisphere. The differences and similarities between the two global circulation models and the various empirical models are outlined and discussed.

1 Introduction

During geomagnetic storms, Joule heating is known to be the dominant solar wind energy dissipation mechanism. Joule heating maximizes in the lower thermosphere-ionosphere (LTI) region, within the 100 to 200 km altitude range, where also current density and conductivity (Pedersen and Hall) maximize. The quantification of Joule heating is a subject of intense research, as it is critical in determining the structure and evolution of the Lower Thermosphere-Ionosphere, and is responsible for a number of effects of societal importance, such as for determining atmospheric drag and predicting the resulting deorbiting times of satellites and space debris within this region. For example, the recent loss of 40 Space-X satellites in February 2022 is thought to have been caused by an underestimate of the enhancement of thermospheric neutral density that resulted from enhanced Joule heating during a moderate geomagnetic storm (Dang et al., 2022; Y. Zhang et al., 2022; Hapgood et al., 2022). It is for this reason that quantifying the heating rates is critical in order to accurately determine satellite drag and orbital lifetime estimations.

Whereas the physics of the collisional processes leading to Joule heating is well understood and is captured in Global Circulation Models (GCMs) of the ionosphere-thermosphere system, the quantification of Joule heating is still largely unknown, and large discrepancies appear between different models and estimation methodologies (Palmroth et al., 2005; Rodger et al., 2001). This is in part because the exact quantification of Joule heating requires the simultaneous and co-located measurement of all relevant parameters that are involved in the calculations of conductivity, electrical currents and fields, and in part because an unknown amount of Joule heating is found in small-scale or sub-grid variability that can not be captured by current models. Also contributing to the above uncertainty, the lower thermosphere-ionosphere (LTI) region, where Joule heating maximizes, is the least sampled of all atmospheric regions (see, e.g., T. Sarris et al. (2023), and references therein): due to the high air drag, the altitude range from ∼100 to 200 km is too high for balloon experiments and too low for current LEO satellites. Thus, the majority of available measurements for this region comes from ground based observatories, such as Incoherent Scatter Radars, and very few in-situ space missions, such as the Atmosphere Explorers of the early 80'. Measurements from the above are used in formulating empirical models of the upper atmosphere, such as the International Reference Ionosphere (IRI) (Bilitza, 2018), NRLMSISE-00 (Picone et al., 2002) and the Hor-

izontal Wind Model (HWM) (Drob et al., 2008). Furthermore, physics-based global circulation Models (GCM), such as the Global Ionosphere/Thermosphere Model (GITM) (Ridley et al., 2006) or the National Center for Atmospheric Research (NCAR) Thermosphere-Ionosphere-Electrodynamics General Circulation Model (TIE-GCM) (Qian et al., 2013) simulate the energetics, dynamics and chemistry of this region. However, there are great discrepancies in geophysical observables describing the basic state of the LTI between empirical models and physics-based models, such as neutral temperature and density, which are largely based on the uncertainty in estimating the amount of Joule heating in the LTI.

Among physics-based models, GITM and TIE-GCM are widely used by the upper atmosphere scientific community. Both are 3D gridded numerical models that are used to simulate the state of the thermosphere and ionosphere in response to external driving by solar wind conditions. GITM and TIE-GCM are both based on a set of equations that describe the physical processes that occur within the thermosphere and ionosphere, such as radiation, convection, and dynamical forcing. From the outputs of these models, which include all essential variables or geophysical observables of the thermosphere and ionosphere, Joule heating can be directly computed at each model grid point.

Together with the above physics-based models, a number of empirical formulations have been derived as proxies of Joule heating, driven by solar and geomagnetic conditions. For example, Joule heating has been found to be closely related to the AE and AL indices (e.g., Perreault and Akasofu (1978); Akasofu (1981); Ahn et al. (1983); Baumjohann and Kamide (1984); Ahn et al. (1989),A. Richmond et al. (1990), Cooper et al. (1995), Lu et al. (1995), Lu et al. (1998). Seasonal and hemispherical differences have been examined as well to establish a more accurate relation between Joule heating and the geomagnetic indices (Nisbet (1982); Lu et al. (1998)). Further to the above, Chun et al. (1999) estimated Joule heating with a quadratic fit to the Polar Cap (PC) index, whereas Knipp et al. (2005) expanded on the work of Chun et al. (1999) by proposing a formula that is based on both the PC and the Disturbance Storm Time (Dst) indices. It is noted that most of the above relations do not take into account the effects of neutral winds, which are known to impact Joule heating significantly (see, e.g., Lu et al. (1995); Emery et al. (1999)).

In this paper Joule heating estimates are presented based on simulation results of the solar storm of 17 March 2015, the largest geomagnetic storm of solar cycle 24 (also known as St Patrick's day 2015 storm). Globally integrated Joule heating rates are calculated in both GITM and TIE-GCM, and are compared against estimates obtained from various empirical formulations. Together with the time series of the evolution of Joule heating during the storm, the cumulative globally integrated Joule heating is compared as calculated by each model. Furthermore, hemispherically-integrated Joule heating rate estimates are compared between GITM and TIE-GCM. It is found that all empirical formulations generally under-estimate the total Joule heating compared to the two GCMs.

This paper is organized as follows: Section 2 presents details of the GITM and TIE-GCM and describes the derivation of Joule heating in both models. Section 3 presents the results of the implementation of the simulations for St Patrick's day 2015 storm as well as the resulting Joule heating as obtained from various empirical formulations. Section 4 discusses the results, highlighting potential causes of the observed discrepancies. Finally, Section 5 summarizes the conclusions of this work.

2 General Circulation Models

2.1 The Global Ionosphere-Thermosphere Model (GITM)

GITM is a non-hydrostatic global circulation model that has been developed in order to simulate the energy balance, chemistry, and dynamics of the Earth's ionosphere

and thermosphere (Ridley et al., 2006; Deng et al., 2019; Vichare et al., 2012). It has also been used to simulate planetary upper atmospheres (Bougher et al., 2015). GITM simulates the state of the mutually coupled ionosphere and thermosphere at altitudes from 100 km to ∼600 km. It solves the coupled continuity, momentum and energy equations of neutrals and ions. The continuity, momentum, and energy equations in GITM have realistic source terms and a contemporary advection solver. Furthermore, GITM solves for the vertical momentum equation, which enables the development of non-hydrostatic solutions and the simulation of more accurate auroral zone dynamics. Each neutral species has a distinct vertical velocity, with a frictional term linking the velocities. Ion species in GITM include: $O^+(4S)$, $O^+(2D)$, $O^+(2P)$, O_2^+, N^+, N_2^+, and NO^+ whereas neutral include: O, O_2, $N(2D)$, $N(2P)$, $N(4S)$, N_2, and NO. A key advantage of GITM compared to other GCMs is that it is capable of employing a versatile, non-uniform grid, with variable resolution in both altitude and latitude, as opposed to a pressure grid that is commonly used in other thermosphere codes. The vertical grid spacing is less than 3 km in the lower thermosphere, at altitudes from 100 to 250 km, whereas it is over 10 km in the upper thermosphere, at altitudes from ∼250 km to 600 km. The ion momentum equation is solved with the assumption of a stable state, while accounting for the pressure, gravity, neutral breezes, and external electric fields. Several high-latitude ionospheric electrodynamic models can be used as external drivers of GITM; these include, among others, the Assimilative Mapping of Ionospheric Electrodynamics (AMIE) approach (A. D. Richmond & Kamide, 1988), the Weimer model (Weimer, 2005), and the Ridley et al. electrodynamic potential pattern (Ridley et al., 2000). GITM model runs are initiated in a number of different ways, such as (1) utilizing an ideal environment in which the user inputs the density and temperature at the base of the atmosphere; (2) using MSIS (Picone et al., 2002) and International Reference Ionosphere (IRI) (Bilitza, 2018); and (3) starting from a prior run. In the present study, the second of the above initialization approaches is followed.

Using the geophysical parameters that are produced as outputs of GITM, Joule heating can then be estimated. These estimations require in addition the computation of electrical current j and Pedersen conductivity, σ_P. The equations that are used in the estimations of the above heating rates are presented in Section 2.3; their derivations are further elaborated in T. Sarris et al. (2022).

2.2 The Thermosphere, Ionosphere, and Electricity General Circulation Model (TIE-GCM)

The NCAR Thermosphere, Ionosphere, and Electricity General Circulation Model (TIE-GCM) is a first-principles, three-dimensional, nonlinear description of the linked thermosphere and ionosphere system with a self-consistent solution of the middle and low-latitude dynamo field (see, e.g., Qian et al. (2013)). The three-dimensional momentum, energy and continuity equations for neutral and ion species are solved at each time-step using a semi-implicit, fourth-order, centered finite difference method on each pressure surface in a staggered vertical grid. The main assumptions used in TIE-GCM calculations include steady-state for the ion and electron energy equations, hydrostatic assumption and constant gravity. A streamlined formulation is used for eddy diffusion. Photoelectron heating is based on a streamlined connection. Simple empirical specifications define the upper boundary requirements for electron heat and flux transfer. Furthermore, TIE-GCM also solves for the vertical momentum equation. Ion species in TIE-GCM include: O^+, O_2^+, N_2^+, NO^+, and N^+ whereas neutral include:O, O_2, NO, $N(4S)$, $N(2D)$. In TIE-GCM, CO_2 is assumed to be in diffusive equilibrium, although it is not explicitly solved. Similarly to GITM, Joule heating is subsequently estimated based on the geophysical parameters that are provided as outputs of TIE-GCM. The equations that are used in the estimations of the above heating rates are further discussed in Section 2.3.

2.3 Derivation of Joule heating rate in TIE-GCM and GITM

In this section the methodology for calculating the Joule heating rates in GITM and TIE-GCM is presented, which is slightly different between the two GCMs: Whereas GITM calculates Joule heating by calculating the complete neutral-ion collisional heating rate, as described in Killeen et al. (1984) and Zhu and Ridley (2016), TIE-GCM follows the approach outlined in Lu et al. (1995). In the following, the equivalence of the two methodologies is derived, highlighting the assumptions used in each methodology. The derivation is initiated by applying the Poynting theorem to the high-latitude ionosphere:

$$\frac{\partial W}{\partial t} + \nabla \cdot \vec{S} + \vec{J} \cdot \vec{E} = 0 \tag{1}$$

where W is the electromagnetic energy density, $\vec{S}$ is the Poynting vector, $\vec{J}$ is the electric current and $\vec{E}$ is the electric field. Neglecting the electromagnetic energy density rate of change by assuming a quasi-steady state, equation (1) becomes:

$$\nabla \cdot \vec{S} + \vec{J} \cdot \vec{E} = 0 \tag{2}$$

The $\vec{J} \cdot \vec{E}$ term is the energy dissipated/generated (Lu et al., 1995). By accounting that the parallel to the ambient magnetic field component of the electric field is much smaller than the perpendicular component ($\vec{E} \approx \vec{E}_\perp$), the $\vec{J} \cdot \vec{E}$ becomes equal to $\vec{J}_\perp \cdot \vec{E}_\perp$.

The ionospheric Joule heating is calculated in the reference frame of the neutral constituents. Thus, by assuming that the neutrals move with a velocity $\vec{u}_n$, the electric field in the reference frame of the neutrals is expressed as:

$$\vec{E}^*_\perp = \vec{E}_\perp + \vec{u}_n \times \vec{B} \tag{3}$$

Thus,

$$\vec{E}_\perp = \vec{E}^*_\perp - \vec{u}_n \times \vec{B} \tag{4}$$

By using equation (4), the electromagnetic energy exchange rate becomes:

$$\vec{J}_\perp \cdot \vec{E}_\perp = \vec{J}_\perp \cdot \vec{E}^*_\perp - \vec{J}_\perp \cdot (\vec{u}_n \times \vec{B}) \tag{5}$$

where the term $\vec{J}_\perp \cdot \vec{E}^*_\perp$ is the Joule heating rate and the term $\vec{J}_\perp \cdot (\vec{u}_n \times \vec{B}$ is the mechanical energy transfer to the neutrals (Lu et al., 1995). Thus, the Joule heating rate can be expressed as:

$$q_{JH} = \vec{J}_\perp \cdot \vec{E}^*_\perp \tag{6}$$

Regarding the electrical current term, applying Ohm's to the ionospheric plasma leads to:

$$\vec{J}_\perp = \vec{J}_P + \vec{J}_H = \sigma_P \vec{E}^*_\perp - \sigma_H (\vec{E}^*_\perp \times \hat{b}) \tag{7}$$

where $\vec{J_P}$ is the Pedersen current, $\vec{J_H}$ is the Hall current, $\hat{b}$ is the unit vector among the ambient magnetic field, and σ_P and σ_H are the Pedersen and Hall conductivities respectively. The Hall current is non-dissipative, and the power transfer is achieved by the Pedersen current; thus, equation (5) becomes:

$$q_{JH} = \vec{J_P} \cdot \vec{E}^*_\perp = (\sigma_P \vec{E}^*_\perp) \cdot \vec{E}^*_\perp = \sigma_P |\vec{E}_\perp + \vec{u}_n \times \vec{B}|^2 \tag{8}$$

Equation (8) is the expression used internally by TIE-GCM for the calculation of Joule heating in the model.

As discussed above, GITM follows a different approach in calculating Joule heating, by calculating the complete neutral-ion collisional heating rate, given as in Killeen et al. (1984) and Zhu and Ridley (2016):

$$q_{JH} = \sum_n n_n m_n \sum_i \frac{\nu_{ni}}{m_i + m_n} [3k_B(T_i - T_n) + m_i(\vec{u}_n - \vec{v}_i)^2] \tag{9}$$

where n_n is the neutral number density, m_n is the neutral mass, m_i is the ion mass, ν_{ni} is the neutral-ion collision frequency, k_B is the Boltzmann constant, T_i and T_n are the ion and neutral temperatures respectively and v_i is the ion velocity.

Subsequently, the equivalence of (8) and (9) with respect to the calculation of Joule heating rates in the ionosphere needs to be shown. By assuming that the ion temperature is in steady state and that the ions are coupled to both the neutrals and electrons, the ion energy equation is derived as:

$$\begin{aligned} 3k_B N_e \frac{m_i}{m_i + m_n} \nu_{in}(T_i - T_n) = N_e \nu_{in} \frac{m_i m_n}{m_i + m_n} (\vec{u}_n - \vec{v}_i)^2 + \\ 3k_B N_e \frac{m_i}{m_i + m_e} \nu_{ie}(T_e - T_i) + N_e \nu_{ie} \frac{m_i m_e}{m_i + m_e} (\vec{u}_e - \vec{v}_i)^2 \end{aligned} \tag{10}$$

Considering $m_e << m_i$, thus $m_i/(m_i + m_e) \approx 1$ and after some manipulations, equation (10) becomes:

$$\begin{aligned} 3k_B \frac{m_i}{m_i + m_n} (T_i - T_n) = \frac{m_i m_n}{m_i + m_n} (\vec{u}_n - \vec{v}_i)^2 + \\ 3k_B \frac{\nu_{ie}}{\nu_{in}} (T_e - T_i) + \frac{\nu_{ie}}{\nu_{in}} m_e (\vec{u}_e - \vec{v}_i)^2 \end{aligned} \tag{11}$$

Collisions between electrons and ions become important (compared to ion-neutral collisions) only in the upper ionosphere, where, however, ions and electrons have almost similar velocities perpendicular to the ambient magnetic field ($E \times B$ drift), thus $\vec{v}_{i\perp} - \vec{v}_{e\perp} \approx 0$. Furthermore, in general, at high latitudes, $\nu_{ie} << \nu_{in}$, and thus (11) becomes:

$$3k_B(T_i - T_n) \approx m_n(\vec{u}_n - \vec{v}_i)^2 \tag{12}$$

By substituting (12) into (9) we get:

$$q_{JH} = \sum_n n_n m_n \sum_i \frac{\nu_{ni}}{m_i + m_n} [m_n(\vec{u}_n - \vec{v}_i)^2 + m_i(\vec{u}_n - \vec{v}_i)^2] \tag{13}$$

Finally, using the relation between ion-neutral and neutral-ion collision frequencies:

$$n_n m_n \nu_{ni} = n_i m_i \nu_{in} \tag{14}$$

equation (13) becomes:

$$q_{JH} = \sum_i n_i m_i \sum_n \nu_{in} (\vec{u}_n - \vec{v}_i)^2 \tag{15}$$

which is the ion-neutral frictional heating rate. The equivalence between the ion-neutral frictional heating rate and the Joule heating rate has been proven in Strangeway (2012), and thus the equivalence of the Joule heating calculation between GITM and TIE-GCM is derived.

The Pedersen conductivity that is needed for the calculation of Joule heating in equation (8) is calculated as:

$$\sigma_P = \frac{q_e}{B} \left[N_{O^+} \frac{r_{O^+}}{1 + r_{O^+}^2} + N_{O_2^+} \frac{r_{O_2^+}}{1 + r_{O_2^+}^2} + N_{NO^+} \frac{r_{NO^+}}{1 + r_{NO^+}^2} + N_e \frac{r_e}{1 + r_e^2} \right] \tag{16}$$

where r_{O^+}, $r_{O_2^+}$, r_{NO^+} and r_e are the collision to gyrofrequency ratios (i.e. $\nu_{i(e)n}/\Omega_{i(e)}$) of O^+, O_2^+, NO^+ and e respectively, which are calculated as described in tables 4.4 and 4.5 of Schunk and Nagy (2009), and N_{O^+}, $N_{O_2^+}$, N_{NO^+} and N_e are the number densities of species in m^{-3}. Collision frequencies of the aforementioned species are calculated for collisions with neutral species of O, O_2 and N_2.

In order to calculate the global heating rates over the same altitude range in the two GCMs, the outputs of each of the two GCMs are first re-gridded with the same altitude resolution and subsequently heating rates are integrated in altitude over the re-grided datasets, from 100km to 600km, and across all magnetic latitudes and longitudes. Further to these calculations, heating rates are also integrated in altitude and are plotted as a function of magnetic latitude and longitude; such altitude-integrated Joule heating rates have also been calculated in a number of prior studies, such as by Lu et al. (1995); Thayer (1998); Weimer (2005) and Deng et al. (2009). In this study, height integrations are performed based a trapezoidal integration scheme, according to:

$$\int_a^b f(x)dx = \sum_{k=1}^{N} \frac{f(x_k - 1) + f(x_k)}{2} \Delta x \tag{17}$$

where f denotes the altitude-resolved quantity that is integrated, x is the altitude, are the a and b are the upper and lower limits of integration respectively and k denotes the provided discrete altitude levels.

Further details on the analysis presented herein can be found in, e.g., T. E. Sarris et al. (2020), T. Sarris et al. (2022) and references therein. The above calculations were performed using the integration module of the open-source code DaedalusMASE (T. Sarris et al., 2022), which has been translated to C++ from the original code that was written in python so as to be more efficient in terms of execution time.

3 Model Runs

GITM and TIE-GCM runs were performed for St Patrick's day storm of March 2015, which is the first and also the largest geomagnetic storm of solar cycle 24. Various aspects of this storm have been described in numerous studies, including, for example, the work of Kanekal et al. (2016) and Hudson et al. (2017) who studied the prompt injection and acceleration of energetic electrons, Jaynes et al. (2018) and Ozeke et al. (2019) who investigated the fast radial diffusion driven by ULF waves, Lyons et al. (2016), Marsal et al. (2017) and Prikryl et al. (2016) who studied ionospheric disturbances induced by energy inputs into the high-latitude regions, Wei et al. (2019), S.-R. Zhang et al. (2017) and Yue et al. (2016) who studied subauroral processes related to magnetosphere-ionosphere coupling, Dmitriev et al. (2017) and Zakharenkova et al. (2016) who studied changes in global neutral wind driven by high-latitude energy and momentum inputs, and D. Zhang et al. (2022) who focused on the generation and propagation of the induced electric field that was responsible for the prompt acceleration of energetic electrons during this storm. In this study, the focus is instead placed on estimating the total Joule heating dissipation during this event, and on investigating discrepancies between GITM, TIE-GCM, as well as various commonly used empirical models.

For consistency, both the GITM and TIE-GCM runs were performed using the same model for high latitude potential estimation, the Weimer model (Weimer, 2005), which is the default electric field specification for both models. The Weimer model uses as inputs the following Interplanetary Magnetic Field (IMF) parameters: plasma density, velocity V_x (along Sun-Earth), and the transverse orientation of the solar wind magnetic field B_y, B_z. In addition, both GITM and TIE-GCM use as input the daily $F10.7$ index, an 81-day average of $F10.7$ and the 3-hourly Kp index. It is noted that TIE-GCM uses the above inputs with a 15-min resolution whereas GITM uses the above inputs with a 1-min resolution. Moreover, GITM requires as input the maximum eastward auroral electrojets strength (SMU), the maximum westward auroral electrojets strength (SML) and the difference between SMU and SML (SME).

In terms of resolution, the TIE-GCM run was performed with a spatial resolution of 2.5 degrees in latitude and longitude, 4 grid points per scale height and a time step of 30 seconds. The GITM run was performed for the same resolution of 2.5 degrees in latitude and longitude, in order to cross-compare simulation results with those of TIE-GCM. The altitude resolution of GITM is 3 grid points per scale height and the temporal resolution is 10 seconds. The resulting output datasets were then converted to a common format for further processing. The datasets and the code are available though Pirnaris et al. (2023). Models Runs were performed on a CPU-based machine with 64GB RAM and an Intel(R) Core(TM) i9-9900K CPU @ 3.60GHz.

Further to the calculation of Joule heating rates in GITM and TIE-GCM, ionospheric dissipation through Joule heating are commonly approximated via empirical formulations that use geomagnetic indices as input. Several studies have derived empirical relationships for the quantification of hemispheric and global Joule heating that are using the AE or AL indices as inputs; these include the studies by Perreault and Akasofu (1978), Akasofu (1981), Ahn et al. (1983), Baumjohann and Kamide (1984), Cooper et al. (1995), Lu et al. (1995). Later on, Chun et al. (1999) estimated Joule heating with a quadratic fit to the Polar Cap (PC) index. Expanding upon the work of Chun et al. (1999), Knipp et al. (2005) proposed an empirical formula based on the PC and the Disturbance Storm Time (Dst) indices. A summary of the above studies and the corresponding relationships as well as constraints in terms of season or hemisphere where these are applicable are presented in Table 1.

An overview of St Patrick's day storm of March 2015 is presented in Figure 1. The storm was caused by a coronal mass ejection that arrived at Earth at ∼04:45 UT, whereas the main phase of the storm began at ∼06:00 UT, indicated by the first vertical dashed

Table 1. Empirical Formulas for Joule Heating Estimations

Study	Formula	Hemisphere	Season
Perreault and Akasofu (1978)	$0.05AE(12)$	-	-
Akasofu (1981)	$0.1AE(12)$	N	Spring
Ahn et al. (1983)	$0.23AE(12)$	N	Spring
Ahn et al. (1983)	$0.19AE(71)$	N	Spring
Ahn et al. (1983)	$0.3AL(12)$	N	Spring
Ahn et al. (1983)	$0.27AL(71)$	N	Spring
Baumjohann and Kamide (1984)	$0.32AE(12)\pm 5$	N	Spring
Baumjohann and Kamide (1984)	$0.33AE(71)\pm 5$	N	Spring
Baumjohann and Kamide (1984)	$0.4AL(71)\pm 5$	N	Spring
Cooper et al. (1995)	$0.54AE(12) - 49$	N	Autumn
Cooper et al. (1995)	$0.28AE(AMIE) - 20$	N	Autumn
Lu et al. (1995)	$0.33AE(12) - 26$	N	Spring
Chun et al. (1999)	$4.14PC^2 + 25PC + 8.9$	-	Equinox
Knipp et al. (2005)	$2.54PC^2 + 29.14PC + 0.21Dst + 0.0023Dst^2$	-	-

*The numbers in parentheses indicate the number of magnetic stations used in the study

line marked as A, when the *Dst* index started to gradually decrease (Figure 1 panel (a)) and the B_z component of the interplanetary magnetic field (IMF) turned southward for the first time (Figure 1 panel (b))). Shortly afterwards, at ∼07:10 UT, the IMF B_z turned northward and then turned negative again at ∼07:30 UT. From ∼10:10 UT to ∼12:20 UT B_z became positive again, leading to a small increase in *Dst*. Finally, at ∼12:20 UT, indicated by the second vertical dashed line marked as B, the IMF B_z turned southward and remained that way until the next day. The *Dst* index continued to decrease, reaching its minimum of -223 nT at ∼23:20 UT on 17 March. This was followed by a long recovery phase. The planetary *Kp* index, also shown in Figure 1 panel (a), reached its maximum value of 7+ to 8- from ∼12 UT to 24 UT.

The *AE* and *AL* indices, at 1 min resolution, are available from the World Data Center(WDC) for Geomagnetism, Kyoto, Japan. The Polar Cap index, at 1 min resolution, consists of the Polar Cap North index (*PCN* index) and the Polar Cap South index (*PCS* index). *PCN* index is taken from the National Space Institute, Technical University of Denmark (DTU, Denmark) and PCS index from the Arctic and Antarctic Research Institute (AARI, Russian Federation). The *Dst* index is provided at 1 hour resolution from WDC, Kyoto, Japan. In order to calculate Joule heating according to Knipp et al. (2005) with a 1 min resolution, we replaced the *Dst* index with the $SYM-H$ index at 1 min resolution from WDC, Kyoto, Japan; as discussed in Wanliss and Showalter (2006), the *Dst* and $SYM-H$ indices are considered equivalent but with different time resolutions. A comparison between the two indices is presented in Figure 1(a). The datasets used in this study are readily available at Pirnaris et al. (2023).

Panels (a) through (e) of Figure 1 present the aggregated driving inputs of GITM and TIE-GCM, as described above, as well as the indices used as inputs for the empirical parameterizations of Joule heating, as follows: Panel (a) presents the *Dst* index (green color), the $SYM-H$ index (dark-cyan color), the 3-hourly *Kp* index (purple) and the $F10.7$ index (blue dashed line). Panel (b) shows the *AL* index (orange) and the *AE* index (cyan). Panel (c) shows the IMF components, B_y (blue) and B_z (brown), in GSM coordinates, for the duration of St Patrick's day storm; the vertical line A marks the first southward turning of B_z, indicating the start of the main phase of the storm, while Line B in the same figure indicates the start of a prolonged period when B_z remains southward; this is further discussed below. Panel (d) presents the solar wind velocity V_x along

the Sun-Earth line (blue solid line) and the plasma density, in units n/cc (brown solid line). Panel (e) presents the maximum eastward auroral electrojet strength (blue solid line), the maximum westward auroral electrojet strength (blue dashed line) and the difference between the two (brown solid line), which are used in driving the GITM model in addition to the inputs shown in panels (a), (d) and (e).

In panel (f) the globally-integrated Joule heating rates are presented as calculated based on the GCMs and the empirical models: The Joule heating rate based on GITM is marked with a thicker dark blue line; Joule heating rate based TIE-GCM is marked with a thicker brown line; and Joule heating rates as estimated according to the various empirical formulations of Table 1 are plotted with the thinner lines, as marked in the inset of figure (in chronological order). It is noted that all the empirical formulas listed in this table give hemispheric estimates of Joule heating; in the results presented in Figure 1 they were multiplied by a factor of 2 to obtain approximations of the global values of Joule heating.

In order to investigate the inter-hemispheric asymmetries between GITM and TIE-GCM, in Figure 2 the integrated Joule Heating are plotted separately over the Northern (panel a) and Southern (panel b) hemispheres. The percentage difference between Joule heating in GITM and TIE-GCM are shown in panel (c), plotted with a solid line for the northern hemisphere and with a dashed line for the southern hemisphere. Finally, in panel (d) the ratio between Joule heating in the northern hemisphere over Joule heating in the southern hemisphere (NH/SH) is plotted separately for GITM (blue line) and TIE-GCM (brown line); these results are further discussed below.

In order to cross-compare the total amount of Joule heating that is deposited onto each thermospheric hemisphere during St Patrick's day storm 2015 as estimated by the two GCMs and the various empirical models, in Figure 3 the cumulative, time-integrated Joule heating is plotted as a function of time. The corresponding models are color-coded and are listed in order of descending Joule heating. The estimated cumulative Joule heating in the northern (southern) hemisphere are plotted in GITM and TIE-GCM with thicker solid (dashed) lines. The thinner lines indicate Joule heating estimates over the northern hemisphere according to the empirical models of Table 1, as marked in the figure's inset. In the cases that empirical estimates are based on indices obtained from 12 ground stations, the results are plotted with a thin solid line, whereas estimates that are based on 71 stations are plotted with a thin dotted line.

4 Discussion

Based on the simulation results shown in Figures 1 and 2 we observe that, even though there is a general order-of-magnitude agreement in the values of the globally-integrated Joule heating rates as obtained through TIE-GCM and GITM in the first part of the storm, up to line B, as well as after the time of minimum *Dst* and in the recovery phase of the storm, after line D, a significant disagreement is observed during the storm main phase, and in particular between lines B and D, both in terms of amplitude as well as in terms of the overall shape and evolution of Joule heating between the two GCMs.

In order to identify the key driving parameters of these discrepancies in Joule heating between the two models, a distance correlation (Richards, 2017) analysis has been performed between the two Joule heating rate time series and each of the input parameter time series shown in panels (a) through (d) of Figure 1. Through the correlation analysis, it is found that Joule heating in GITM is strongly driven by the *SME* electrojet strength, with a correlation coefficient of 0.70; the correlation of *SME* with TIEGCM is 0.54, although it is noted that *SME* is not used as an input in TIE-GCM. In comparison, the correlation coefficient of GITM and TIE-GCM with B_y is 0.27 and 0.21, respectively, and the correlation with B_z is -0.36 and -0.24, respectively. The negative sign in-

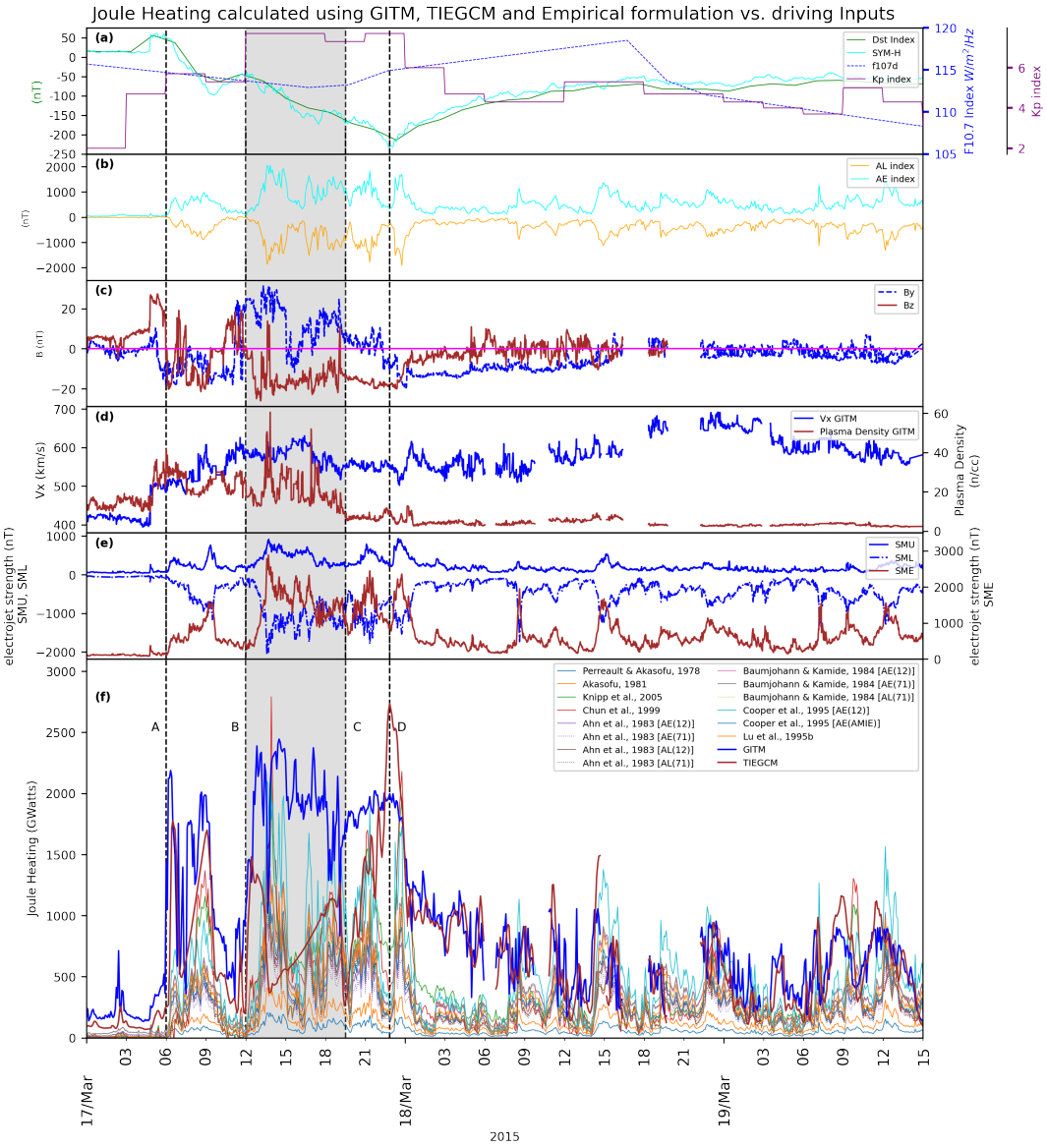

Figure 1. Joule Heating in combination with Geophysical Indices and used quantities

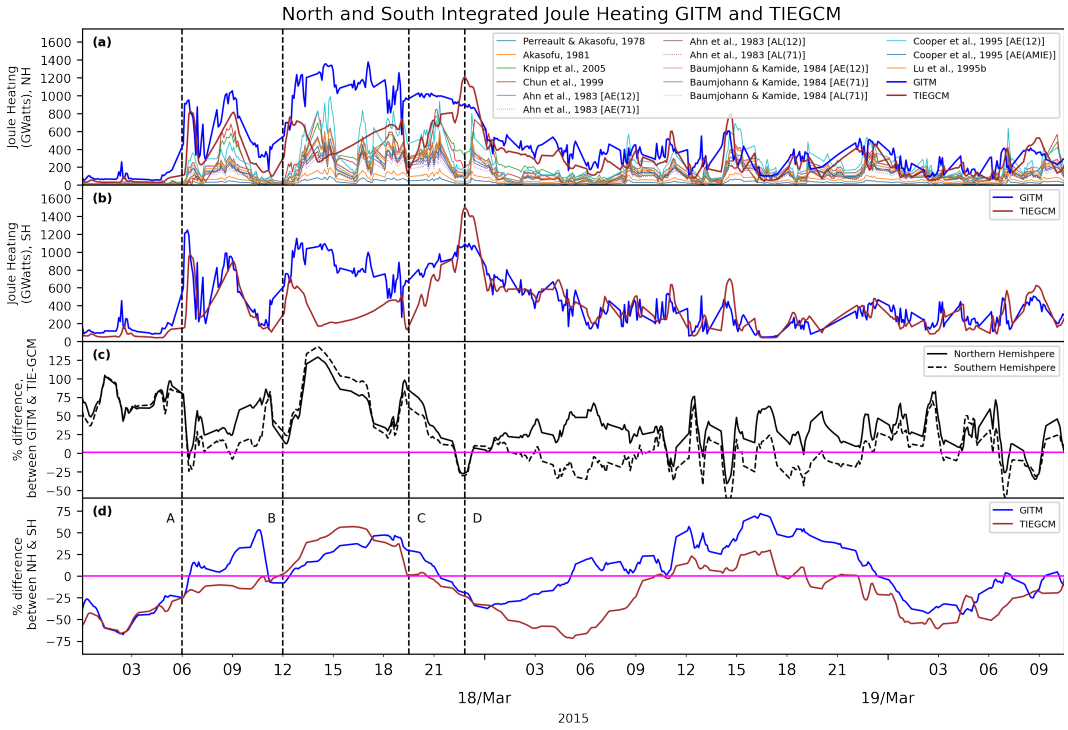

Figure 2. Integrated Joule Heating time-series per Hemisphere, North 63° to 90° deg and South -63° to -90°

dicates an anti-correlation between Joule heating and B_z, which is attributed to the enhanced Joule heating during southward turnings of the IMF. The dependence of Joule heating on B_z has been examined in more detail in various studies, such as, e.g., by McHarg et al. (2005).

The differences in the resulting Joule heating due to the different driving conditions are evident in particular in the period from ∼13:30UT to ∼16:30UT on March 17, 2015, shown in the gray-shaded region that is bounded by lines B and C. During this time, it can be seen that GITM is well correlated with the *SME* electrojet strength, with an increase and subsequent decrease in *SME* being accompanied by a corresponding increase followed by a gradual decrease in Joule heating, whereas, in contrast, Joule heating in TIE-GCM shows an initial drop followed by a gradual increase. This increase appears to be well-correlated with the prolonged southward turning of IMF B_z during this time, which does not appear to affect in the same way the calculations of Joule heating in GITM.

An additional striking difference between GITM and TIE-GCM is a clear correlation between the peak of Joule heating and the minimum *Dst* in TIE-GCM, marked with line D, whereas GITM does not seem to follow a similar correlation with *Dst*. Furthermore, TIE-GCM demonstrates a larger variability compared to GITM, as indicated by the larger peak-to-peak fluctuation amplitudes. It is speculated that this is due to the large number of southward B_z turnings during this event, which, as discussed above, appears to affect to a larger extent the calculations of Joule heating in TIE-GCM rather than in GITM.

Comparing the magnitudes of the two Joule heating estimates between the two GCMs as shown in Figure 2(a) and (b), it is found that the two estimates are in closer agreement in the initial phase of the storm, but that subsequently, after the southward turning of B_z and the increase of *Kp* from 4 to 8-, GITM estimates are almost consistently

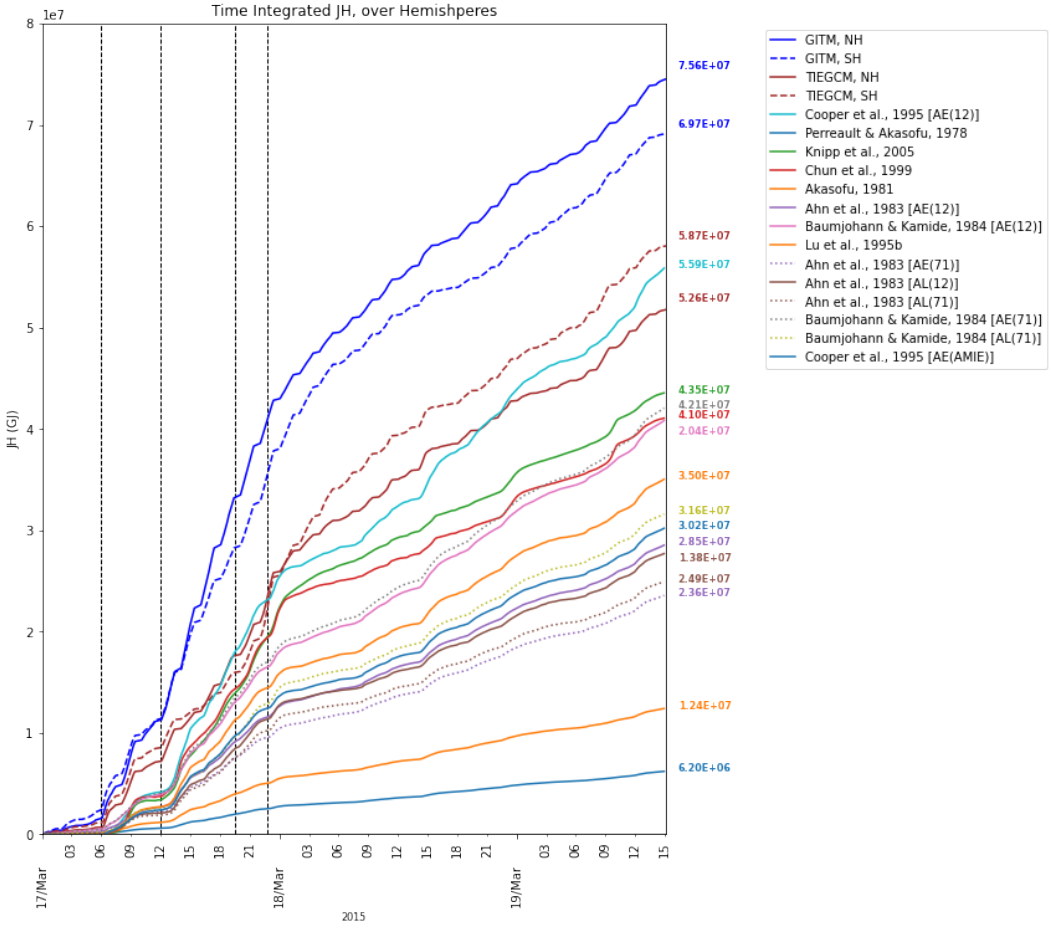

Figure 3. Time-integrated (cumulative) global Joule heating according to GITM, TIE-GCM and various empirical models, as marked, listed from highest to lowest Joule heating values.

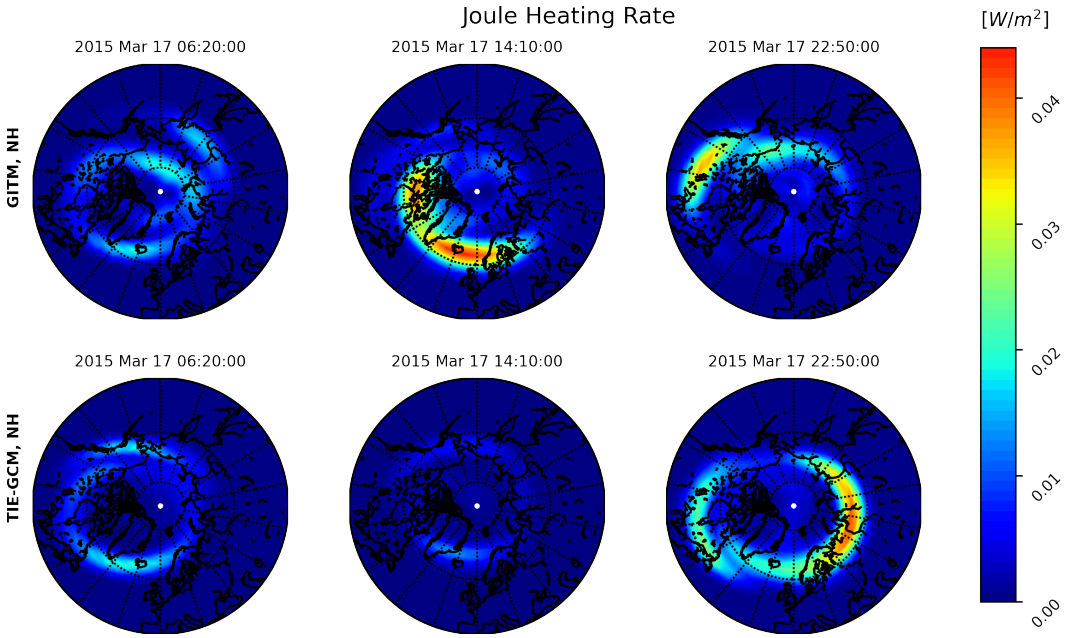

Figure 4. Height-integrated Joule Heating as calculated in GITM (top) and TIE-GCM (bottom) over the northern hemisphere for three different snapshots during St. Patricks day event, as marked.

higher that those of TIEGCM, reaching a maximum percentage difference of $\sim$ 143% on 17 March 2015, 14:10 UT as shown in Figure 2(c), with the exception of the short time period around the minimum *Dst*, observed on 17 March 2015, 22:50 UT (vertical dashed line D), when Joule heating in TIE-GCM exceeds the values of GITM by $\sim$ 30%. It is noted that even higher (in absolute value) percentage differences of Joule heating appear between TIE-GCM and GITM later on during the recovery phase on 18 and 19 March 2015, even though these large percentage differences and their large fluctuations are due to the very low values of Joule heating that are observed during the recovery phase.

In Figure 4 a polar plot of the height-integrated Joule heating over the northern hemisphere as a function of geographic latitude and longitude, based GITM (top panels) and TIE-GCM (lower panels), is presented. Three characteristic snapshots during St Patrick's day storm are plotted: the left-hand side panels are from 17 March 2015 at 06:20 UT, and correspond to the beginning of the storm, which is characterized by a close agreement in the magnitude of Joule heating from the two models. The middle panels are from 17 March 2015 at 14:10 UT, and correspond to the time of maximum percentage difference in Joule heating from GITM compared to TIE-GCM; this time corresponds to the peak of the solid and dashed black lines in Figure 2 (c). Finally, the right-hand side panels of Figure 4 are from 17 March 2015 at 22:50 UT, and correspond to line D, which marks the peak of the storm, as indicated by the minimum in *Dst*. During this time, the maximum value of Joule heating appears in TIE-GCM, exceeding the corresponding value in GITM, as indicated by the local negative peak of the solid and dashed black lines in Figure 2 (c) at this time. The comparisons between the top and lower panels of Figure 4 show that, besides the differences in the amplitude of Joule heating between GITM and TIE-GCM and the correlation of Joule heating with different driving parameters, there is also significant difference in the distribution of Joule heating in longitude and latitude, with markedly different localization and extent of the structures where Joule heating appears.

Comparing the time series of Joule heating from the two GCMs with the corresponding values from the empirical models in Figure 2(a), it can be seen that there is a closer agreement between the empirical models and TIE-GCM rather than with GITM.

Comparing the percentage difference between the hemispherically-integrated Joule heating in the northern and southern hemispheres that is plotted in Figure 2(d), it can be seen that TIE-GCM shows on average larger inter-hemispheric asymmetry than GITM during times of enhanced Joule heating, reaching up to $\sim 60\%$ higher Joule heating in the northern hemisphere and up to $\sim 75\%$ higher Joule heating in the southern hemisphere in the recovery phase of the storm; in comparison, GITM shows $\sim 50\%$ higher Joule heating in the northern hemisphere during the peak of the storm and up to $\sim 25\%$ higher Joule heating in the southern hemisphere in the descending phase. A striking difference between the two models is revealed through the hemispherically-integrated, time-integrated (cumulative) Joule heating, plotted in Figure 3: whereas in GITM a larger amount of Joule heating is deposited in the northern hemisphere, in TIE-GCM the largest amount is deposited in the southern hemisphere. A conclusive explanation for this discrepancy can not be provided as part of this investigation, nor can a conclusion be drawn on the relative level of accuracy, but these results point to the need for a more detailed investigation.

With respect to the causes of the inter-hemispheric differences, it is noted that solar EUV radiation, which is generally known to produce inter-hemispheric asymmetries in the Ionosphere-Thermosphere system, is hemispherically symmetric during this event, as the St Patrick's day storm of March 2015 took place at a time that is close to the Spring equinox. Instead, the observed differences are most probably associated with the Earth's asymmetric magnetic field configuration: for example, as discussed in, e.g., Laundal et al. (2017) and references therein, the dipole tilt and eccentricity shift in the Earth's magnetic field lead to a displacement between the geographic and geomagnetic poles, which is larger in the southern hemisphere, and to a difference in the magnetic field strength between north-south conjugated latitudes. Such asymmetries have been discussed by, e.g., Hong et al. (2021), who also used GITM to study the impacts of different causes on the inter-hemispheric asymmetry of the ionosphere-thermosphere system, including inter-hemispheric differences associated with the solar irradiance, the geomagnetic field, and the magnetospheric forcing under moderate geomagnetic conditions. Hong et al. (2021) also derived an index of inter-hemispheric asymmetry for Joule heating, which, for solar equinox conditions such as studied herein, was found to be as large as $\sim 43\%$ due to the asymmetric geomagnetic field, $\sim 28\%$ due to asymmetric particle precipitation and $\sim 35\%$ due to asymmetric ion convection pattern. It is noted that, as discussed above, both GITM and TIE-GCM use the IGRF magnetic field model, and hence the asymmetries in the magnetic field are the same; thus the differences in the observed behavior are more likely attributed to the asymmetric particle precipitation and the asymmetric ion convection pattern. However the exact causes of the different behavior of TIE-GCM and GITM with respect to the inter-hemispheric differences is a subject of further research.

5 Summary and Conclusions

Based on GITM, TIE-GCM and various empirical formulations, globally integrated heating rates are calculated during St Patrick's day storm of 2015. It is found that Joule heating rate estimates in the global circulation models, GITM and TIE-GCM, are generally higher in magnitude than all empirical models. Comparing GITM and TIE-GCM, it is found that Joule heating has higher amplitudes and also a smaller peak-to-peak variability in GITM than in TIE-GCM. Through correlation analysis, and also by comparing the heating rates for a period of clear anti-correlation in the heating rate trend between the two models, it is found that GITM is strongly driven by the *SME* index, which is not present in TIE-GCM, and that Joule heating in TIE-GCM is affected by southward turnings of B_z to a much larger extent than GITM.

By integrating the Joule heating estimates separately in each hemisphere, it is found that GITM shows a larger degree of asymmetry during the main phase of the storm than TIE-GCM. Furthermore, by integrating Joule heating in time it is found that the total, cumulative Joule heating input to the thermosphere is larger in GITM, followed by TIE-GCM and then by the various empirical models, with the percentage differences starting from $\sim 28\%$ (GITM vs. TIE-GCM) and $\sim 56\%$ (GITM vs. the model by (Cooper et al., 1995)). Interestingly, whereas higher Joule heating is found to be deposited cumulatively over the duration of the storm in the northern hemisphere in GITM, inversely, higher Joule heating is deposited in the southern hemisphere in TIE-GCM; the results of this discrepancy are a subject of further investigation. Furthermore, the localization (latitudinal and longitudinal distribution) of Joule heating is largely different in the two models.

In conclusion, as also demonstrated by the discrepancies in the above cross-comparisons between empirical and physics-based models, Joule heating remains to this date a quantity with many discrepancies in its estimation, showing large gaps in its understanding and parameterization. At the same time, it is a quantity of great significance in LTI processes, as it determines to a great extent the overall energy budget, in particular during active solar and geomagnetic conditions. Thus, characterizing its magnitude, time evolution and variability within the latitude and altitude region where it maximizes and accurately parameterizing Joule heating by solar and geomagnetic conditions are critical missing pieces in accurately understanding and modeling LTI processes. This demonstrates the currently limited knowledge about Joule heating and emphasizes the need for comprehensive measurements, such as outlined in T. Sarris et al. (2023), to accurately quantify Joule heating.

6 Open Research

The netCDF type data used for integrated Joule heating in the study are available at ZENODO via `10.5281/zenodo.7716871` with Creative Common Attribution 4.0 International licence. Space indices files are delivered by OMNIWEB and SuperMAG and included in the aforementioned dataset.

Software used for calculation of Joule Heating is preserved at `10.5281/zenodo.7716871`, available via Creative Common Attribution 4.0 International licence and developed openly using Python and Fortran.

Code and Data of this project is available on Pirnaris et al. (2023)

References

Ahn, B.-H., Akasofu, S.-I., & Kamide, Y. (1983). The joule heat production rate and the particle energy injection rate as a function of the geomagnetic indices ae and al. *Journal of Geophysical Research: Space Physics*, *88*(A8), 6275–6287.

Ahn, B.-H., Kroehl, H., Kamide, Y., & Gorney, D. (1989). Estimation of ionospheric electrodynamic parameters using ionospheric conductance deduced from bremsstrahlung x ray image data. *Journal of Geophysical Research: Space Physics*, *94*(A3), 2565–2586.

Akasofu, S. I. (1981). Energy coupling between the solar wind and the magnetosphere. *Space Science Reviews*, *28*, 121–190.

Baumjohann, W., & Kamide, Y. (1984). Hemispherical joule heating and the ae indices. *Journal of Geophysical Research: Space Physics*, *89*(A1), 383–388.

Bilitza, D. (2018). Iri the international standard for the ionosphere. *Advances in Radio Science*, *16*, 1–11. Retrieved from `https://ars.copernicus.org/articles/16/1/2018/` doi: 10.5194/ars-16-1-2018

Bougher, S. W., Pawlowski, D., Bell, J. M., Nelli, S., McDunn, T., Murphy, J. R.,

... Ridley, A. (2015). Mars global ionosphere-thermosphere model: Solar cycle, seasonal, and diurnal variations of the mars upper atmosphere. *Journal of Geophysical Research: Planets*, *120*(2), 311-342. Retrieved from https://agupubs.onlinelibrary.wiley.com/doi/abs/10.1002/2014JE004715 doi: https://doi.org/10.1002/2014JE004715

Chun, F. K., Knipp, D. J., McHarg, M. G., Lu, G., Emery, B. A., Vennerstrøm, S., & Troshichev, O. A. (1999). Polar cap index as a proxy for hemispheric joule heating. *Geophysical research letters*, *26*(8), 1101–1104.

Cooper, M., Clauer, C., Emery, B., Richmond, A., & Winningham, J. (1995). A storm time assimilative mapping of ionospheric electrodynamics analysis for the severe geomagnetic storm of november 8–9, 1991. *Journal of Geophysical Research: Space Physics*, *100*(A10), 19329–19342.

Dang, T., Li, X., Luo, B., Li, R., Zhang, B., Pham, K., ... Wang, Y. (2022). Unveiling the space weather during the starlink satellites destruction event on 4 february 2022. *Space Weather*, *20*(8), e2022SW003152. Retrieved from https://agupubs.onlinelibrary.wiley.com/doi/abs/10.1029/2022SW003152 (e2022SW003152 2022SW003152) doi: https://doi.org/10.1029/2022SW003152

Deng, Y., Heelis, R., Lyons, L., Nishimura, Y., & Gabrielse, C. (2019, 12). Impact of flow bursts in the auroral zone on the ionosphere and thermosphere. *Journal of Geophysical Research: Space Physics*, *124*. doi: 10.1029/2019JA026755

Deng, Y., Maute, A., Richmond, A. D., & Roble, R. G. (2009). Impact of electric field variability on joule heating and thermospheric temperature and density. *Geophysical Research Letters*, *36*(8). Retrieved from https://agupubs.onlinelibrary.wiley.com/doi/abs/10.1029/2008GL036916 doi: https://doi.org/10.1029/2008GL036916

Dmitriev, A. V., Suvorova, A. V., Klimenko, M. V., Klimenko, V. V., Ratovsky, K. G., Rakhmatulin, R. A., & Parkhomov, V. A. (2017). Predictable and unpredictable ionospheric disturbances during st. patrick's day magnetic storms of 2013 and 2015 and on 8–9 march 2008. *Journal of Geophysical Research: Space Physics*, *122*(2), 2398-2423. Retrieved from https://agupubs.onlinelibrary.wiley.com/doi/abs/10.1002/2016JA023260 doi: https://doi.org/10.1002/2016JA023260

Drob, D. P., Emmert, J. T., Crowley, G., Picone, J. M., Shepherd, G. G., Skinner, W., ... Vincent, R. A. (2008). An empirical model of the earth's horizontal wind fields: Hwm07. *Journal of Geophysical Research: Space Physics*, *113*(A12). Retrieved from https://agupubs.onlinelibrary.wiley.com/doi/abs/10.1029/2008JA013668 doi: https://doi.org/10.1029/2008JA013668

Emery, B., Lathuillere, C., Richards, P., Roble, R., Buonsanto, M., Knipp, D., ... Niciejewski, R. (1999). Time dependent thermospheric neutral response tothe 2–11 november 1993 storm period. *Journal of Atmospheric and Solar-Terrestrial Physics*, *61*(3), 329-350. Retrieved from https://www.sciencedirect.com/science/article/pii/S1364682698001370 doi: https://doi.org/10.1016/S1364-6826(98)00137-0

Hapgood, M., Liu, H., & Lugaz, N. (2022). Spacex—sailing close to the space weather? *Space Weather*, *20*(3), e2022SW003074. Retrieved from https://agupubs.onlinelibrary.wiley.com/doi/abs/10.1029/2022SW003074 (e2022SW003074 2022SW003074) doi: https://doi.org/10.1029/2022SW003074

Hong, Y., Deng, Y., Zhu, Q., Maute, A., Sheng, C., Welling, D., & Lopez, R. (2021, November). Impacts of different causes on the inter-hemispheric asymmetry of ionosphere-thermosphere system at mid- and high-latitudes: GITM simulations. *Space Weather*, *19*(11). Retrieved from https://doi.org/10.1029/2021sw002856 doi: 10.1029/2021sw002856

Hudson, M., Jaynes, A., Kress, B., Li, Z., Patel, M., Shen, X.-C., ... Wygant,

J. (2017). Simulated prompt acceleration of multi-mev electrons by the 17 march 2015 interplanetary shock. *Journal of Geophysical Research: Space Physics*, *122*(10), 10,036-10,046. Retrieved from https://agupubs.onlinelibrary.wiley.com/doi/abs/10.1002/2017JA024445 doi: https://doi.org/10.1002/2017JA024445

Jaynes, A. N., Ali, A. F., Elkington, S. R., Malaspina, D. M., Baker, D. N., Li, X., ... Wygant, J. R. (2018). Fast diffusion of ultrarelativistic electrons in the outer radiation belt: 17 march 2015 storm event. *Geophysical Research Letters*, *45*(20), 10,874-10,882. Retrieved from https://agupubs.onlinelibrary.wiley.com/doi/abs/10.1029/2018GL079786 doi: https://doi.org/10.1029/2018GL079786

Kanekal, S. G., Baker, D. N., Fennell, J. F., Jones, A., Schiller, Q., Richardson, I. G., ... Wygant, J. R. (2016). Prompt acceleration of magnetospheric electrons to ultrarelativistic energies by the 17 march 2015 interplanetary shock. *Journal of Geophysical Research: Space Physics*, *121*(8), 7622-7635. Retrieved from https://agupubs.onlinelibrary.wiley.com/doi/abs/10.1002/2016JA022596 doi: https://doi.org/10.1002/2016JA022596

Killeen, T., Hays, P., Carignan, G., Heelis, R., Hanson, W., Spencer, N., & Brace, L. (1984). Ion-neutral coupling in the high-latitude f region: Evaluation of ion heating terms from dynamics explorer 2. *Journal of Geophysical Research: Space Physics*, *89*(A9), 7495–7508.

Knipp, D., Welliver, T., McHarg, M., Chun, F., Tobiska, W., & Evans, D. (2005). Climatology of extreme upper atmospheric heating events. *Advances in Space Research*, *36*(12), 2506–2510.

Laundal, K. M., Cnossen, I., Milan, S. E., Haaland, S. E., Coxon, J., Pedatella, N. M., ... Reistad, J. P. (2017, July). North–south asymmetries in earth's magnetic field. *Space Science Reviews*, *206*(1-4), 225–257. Retrieved from https://doi.org/10.1007/s11214-016-0273-0 doi: 10.1007/s11214-016-0273-0

Lu, G., Pi, X., Richmond, A. D., & Roble, R. G. (1998, February). Variations of total electron content during geomagnetic disturbances: A model/observation comparison. *Geophysical Research Letters*, *25*(3), 253–256. Retrieved from https://doi.org/10.1029/97gl03778 doi: 10.1029/97gl03778

Lu, G., Richmond, A., Emery, B., & Roble, R. (1995). Magnetosphere-ionosphere-thermosphere coupling: Effect of neutral winds on energy transfer and field-aligned current. *Journal of Geophysical Research: Space Physics*, *100*(A10), 19643–19659.

Lyons, L. R., Gallardo-Lacourt, B., Zou, S., Weygand, J. M., Nishimura, Y., Li, W., ... Nishitani, N. (2016). The 17 march 2013 storm: Synergy of observations related to electric field modes and their ionospheric and magnetospheric effects. *Journal of Geophysical Research: Space Physics*, *121*(11), 10,880-10,897. Retrieved from https://agupubs.onlinelibrary.wiley.com/doi/abs/10.1002/2016JA023237 doi: https://doi.org/10.1002/2016JA023237

Marsal, S., Torta, J. M., Segarra, A., & Araki, T. (2017). Use of spherical elementary currents to map the polar current systems associated with the geomagnetic sudden commencements on 2013 and 2015 st. patrick's day storms. *Journal of Geophysical Research: Space Physics*, *122*(1), 194-211. Retrieved from https://agupubs.onlinelibrary.wiley.com/doi/abs/10.1002/2016JA023166 doi: https://doi.org/10.1002/2016JA023166

McHarg, M., Chun, F., Knipp, D., Lu, G., Emery, B., & Ridley, A. (2005). High-latitude joule heating response to imf inputs. *Journal of Geophysical Research: Space Physics*, *110*(A8). Retrieved from https://agupubs.onlinelibrary.wiley.com/doi/abs/10.1029/2004JA010949 doi: https://doi.org/10.1029/2004JA010949

Nisbet, J. (1982). Relations between the birkeland currents, the auroral electrojet

indices and high latitude joule heating. *Journal of Atmospheric and Terrestrial Physics*, *44*(9), 797-809. Retrieved from https://www.sciencedirect.com/science/article/pii/0021916982900095 doi: https://doi.org/10.1016/0021-9169(82)90009-5

Ozeke, L. G., Mann, I. R., Claudepierre, S. G., Henderson, M., Morley, S. K., Murphy, K. R., ... Baker, D. N. (2019). The march 2015 superstorm revisited: Phase space density profiles and fast ulf wave diffusive transport. *Journal of Geophysical Research: Space Physics*, *124*(2), 1143-1156. Retrieved from https://agupubs.onlinelibrary.wiley.com/doi/abs/10.1029/2018JA026326 doi: https://doi.org/10.1029/2018JA026326

Palmroth, M., Janhunen, P., Pulkkinen, T. I., Aksnes, A., Lu, G., Østgaard, N., ... Germany, G. A. (2005). Assessment of ionospheric joule heating by gumics-4 mhd simulation, amie, and satellite-based statistics: towards a synthesis. *Annales Geophysicae*, *23*(6), 2051–2068. Retrieved from https://angeo.copernicus.org/articles/23/2051/2005/ doi: 10.5194/angeo-23-2051-2005

Perreault, P., & Akasofu, S. I. (1978, 09). A study of geomagnetic storms. *Geophysical Journal International*, *54*(3), 547-573. Retrieved from https://doi.org/10.1111/j.1365-246X.1978.tb05494.x doi: 10.1111/j.1365-246X.1978.tb05494.x

Picone, J. M., Hedin, A. E., Drob, D. P., & Aikin, A. C. (2002). Nrlmsise-00 empirical model of the atmosphere: Statistical comparisons and scientific issues. *Journal of Geophysical Research: Space Physics*, *107*(A12), SIA 15-1-SIA 15-16. Retrieved from https://agupubs.onlinelibrary.wiley.com/doi/abs/10.1029/2002JA009430 doi: https://doi.org/10.1029/2002JA009430

Pirnaris, P., Sarris, T. E., & Tourgaidis, S. (2023). *Joule heating calculation during st patrick's day storm of march 2015* [dataset]. Zenodo. Retrieved from https://www.unavco.org/data/doi/10.7283/633E-1497 doi: 10.5281/zenodo.7716871

Prikryl, P., Ghoddousi-Fard, R., Weygand, J. M., Viljanen, A., Connors, M., Danskin, D. W., ... Sreeja, V. (2016). Gps phase scintillation at high latitudes during the geomagnetic storm of 17–18 march 2015. *Journal of Geophysical Research: Space Physics*, *121*(10), 10,448-10,465. Retrieved from https://agupubs.onlinelibrary.wiley.com/doi/abs/10.1002/2016JA023171 doi: https://doi.org/10.1002/2016JA023171

Qian, L., Burns, A., Emery, B., Foster, B., Lu, G., Maute, A., ... Wang, W. (2013, 01). The ncar tie-gcm: A community model of the coupled thermosphere/ionosphere system. *Geophysical Monograph Series*, *201*, 73-83. doi: 10.1029/2012GM001297

Richards, D. S. P. (2017). Distance correlation: A new tool for detecting association and measuring correlation between data sets. *arXiv: Other Statistics*.

Richmond, A., Kamide, Y., Akasofu, S.-I., Alcaydé, D., Blanc, M., De la Beaujardière, O., ... others (1990). Global measures of ionospheric electrodynamic activity inferred from combined incoherent scatter radar and ground magnetometer observations. *Journal of Geophysical Research: Space Physics*, *95*(A2), 1061–1071.

Richmond, A. D., & Kamide, Y. (1988). Mapping electrodynamic features of the high-latitude ionosphere from localized observations: Technique. *Journal of Geophysical Research: Space Physics*, *93*(A6), 5741-5759. Retrieved from https://agupubs.onlinelibrary.wiley.com/doi/abs/10.1029/JA093iA06p05741 doi: https://doi.org/10.1029/JA093iA06p05741

Ridley, A., Crowley, G., & Freitas, C. (2000). An empirical model of the ionospheric electric potential. *Geophysical research letters*, *27*(22), 3675–3678.

Ridley, A., Deng, Y., & Tóth, G. (2006). The global ionosphere–thermosphere model. *Journal of Atmospheric and Solar-Terrestrial Physics*, *68*(8), 839-864.

Retrieved from https://www.sciencedirect.com/science/article/pii/S1364682606000071 doi: https://doi.org/10.1016/j.jastp.2006.01.008

Rodger, A. S., Wells, G. D., Moffett, R. J., & Bailey, G. J. (2001). The variability of joule heating, and its effects on the ionosphere and thermosphere. *Annales Geophysicae*, *19*(7), 773–781. Retrieved from https://angeo.copernicus.org/articles/19/773/2001/ doi: 10.5194/angeo-19-773-2001

Sarris, T., Palmroth, M., Aikio, A., Buchert, S. C., Clemmons, J., Clilverd, M., ... Yamauchi, M. (2023). Plasma-neutral interactions in the lower thermosphere-ionosphere: The need for in situ measurements to address focused questions. *Frontiers in Astronomy and Space Sciences*, *9*. Retrieved from https://www.frontiersin.org/articles/10.3389/fspas.2022.1063190 doi: 10.3389/fspas.2022.1063190

Sarris, T., Tourgaidis, S., & Pirnaris, P. (2022). Daedalus mase (mission assessment through simulation exercise): a toolset for analysis of in situ missions and for processing global circulation model outputs in the lower thermosphere-ionosphere. *Frontiers*, *submitted*.

Sarris, T. E., Talaat, E. R., Palmroth, M., Dandouras, I., Armandillo, E., Kervalishvili, G., ... Aikio, A. (2020). Daedalus: a low-flying spacecraft for in situ exploration of the lower thermosphere–ionosphere. *Geoscientific Instrumentation, Methods and Data Systems*, *9*(1), 153–191. Retrieved from https://gi.copernicus.org/articles/9/153/2020/ doi: 10.5194/gi-9-153-2020

Schunk, R., & Nagy, A. (2009). *Ionospheres: Physics, plasma physics, and chemistry* (2nd ed.). Cambridge University Press. doi: 10.1017/CBO9780511635342

Strangeway, R. J. (2012). The equivalence of joule dissipation and frictional heating in the collisional ionosphere. *Journal of Geophysical Research: Space Physics*, *117*(A2). doi: https://doi.org/10.1029/2011JA017302

Thayer, J. P. (1998). Height-resolved joule heating rates in the high-latitude e region and the influence of neutral winds. *Journal of Geophysical Research: Space Physics*, *103*(A1), 471-487. Retrieved from https://agupubs.onlinelibrary.wiley.com/doi/abs/10.1029/97JA02536 doi: https://doi.org/10.1029/97JA02536

Vichare, G., Ridley, A., & Yiğit, E. (2012, 05). Quiet-time low latitude ionospheric electrodynamics in the non-hydrostatic global ionosphere-thermosphere model. *Journal of Atmospheric and Solar-Terrestrial Physics*, *80*, 161-172. doi: 10.1016/j.jastp.2012.01.009

Wanliss, J. A., & Showalter, K. M. (2006). High-resolution global storm index: Dst versus sym-h. *Journal of Geophysical Research: Space Physics*, *111*(A2).

Wei, D., Yu, Y., & He, F. (2019). The magnetospheric driving source of double-peak subauroral ion drifts: Double ring current pressure peaks. *Geophysical Research Letters*, *46*(13), 7079-7087. Retrieved from https://agupubs.onlinelibrary.wiley.com/doi/abs/10.1029/2019GL083186 doi: https://doi.org/10.1029/2019GL083186

Weimer, D. R. (2005). Improved ionospheric electrodynamic models and application to calculating joule heating rates. *Journal of Geophysical Research: Space Physics*, *110*(A5). Retrieved from https://agupubs.onlinelibrary.wiley.com/doi/abs/10.1029/2004JA010884 doi: https://doi.org/10.1029/2004JA010884

Yue, X., Wan, W., Liu, L., Liu, J., Zhang, S., Schreiner, W. S., ... Hu, L. (2016). Mapping the conjugate and corotating storm-enhanced density during 17 march 2013 storm through data assimilation. *Journal of Geophysical Research: Space Physics*, *121*(12), 12,202-12,210. Retrieved from https://agupubs.onlinelibrary.wiley.com/doi/abs/10.1002/2016JA023038 doi: https://doi.org/10.1002/2016JA023038

Zakharenkova, I., Astafyeva, E., & Cherniak, I. (2016). Gps and glonass observations

of large-scale traveling ionospheric disturbances during the 2015 st. patrick's day storm. *Journal of Geophysical Research: Space Physics*, *121*(12), 12,138-12,156. Retrieved from https://agupubs.onlinelibrary.wiley.com/doi/abs/10.1002/2016JA023332 doi: https://doi.org/10.1002/2016JA023332

Zhang, D., Liu, W., Du, J., Yu, Y., Li, X., & Sarris, T. (2022, 10). Response of electric field in terrestrial magnetosphere to interplanetary shock. *The Astrophysical Journal*, *938*. doi: 10.3847/1538-4357/ac90cc

Zhang, S.-R., Erickson, P. J., Zhang, Y., Wang, W., Huang, C., Coster, A. J., ... Kerr, R. (2017). Observations of ion-neutral coupling associated with strong electrodynamic disturbances during the 2015 st. patrick's day storm. *Journal of Geophysical Research: Space Physics*, *122*(1), 1314-1337. Retrieved from https://agupubs.onlinelibrary.wiley.com/doi/abs/10.1002/2016JA023307 doi: https://doi.org/10.1002/2016JA023307

Zhang, Y., Paxton, L. J., Schaefer, R., & Swartz, W. H. (2022). Thermospheric conditions associated with the loss of 40 starlink satellites. *Space Weather*, *20*(10), e2022SW003168. Retrieved from https://agupubs.onlinelibrary.wiley.com/doi/abs/10.1029/2022SW003168 (e2022SW003168 2022SW003168) doi: https://doi.org/10.1029/2022SW003168

Zhu, J., & Ridley, A. J. (2016). Investigating the performance of simplified neutral-ion collisional heating rate in a global it model. *Journal of Geophysical Research: Space Physics*, *121*(1), 578–588.